Inorganic Chemistry

pubs.acs.org/IC Article

Influence of Composition and Structure on the Optoelectronic Properties of Photocatalytic Bi_4NbO_8Cl–Bi_2GdO_4Cl Intergrowths

Nayana Christudas Beena, Nicolas P. L. Magnard, Danilo Puggioni, Roberto dos Reis, Kaustav Chatterjee, Xun Zhan, Vinayak P. Dravid, James M. Rondinelli, Kirsten M. Ø. Jensen, and Sara E. Skrabalak*

Cite This: *Inorg. Chem.* 2024, 63, 8131–8141 Read Online

ACCESS | Metrics & More | Article Recommendations | Supporting Information

ABSTRACT: Mixed metal oxyhalides are an exciting class of photocatalysts, capable of the sustainable generation of fuels and remediation of pollutants with solar energy. Bismuth oxyhalides of the types Bi_4MO_8X (M = Nb and Ta; X = Cl and Br) and Bi_2AO_4X (A = most lanthanides; X = Cl, Br, and I) have an electronic structure that imparts photostability, as their valence band maxima (VBM) are composed of O 2p orbitals rather than X *n*p orbitals that typify many other bismuth oxyhalides. Here, flux-based synthesis of intergrowth Bi_4NbO_8Cl–Bi_2GdO_4Cl is reported, testing the hypothesis that both intergrowth stoichiometry and M identity serve as levers toward tunable optoelectronic properties. X-ray scattering and atomically resolved electron microscopy verify intergrowth formation. Facile manipulation of the Bi_4NbO_8Cl-to-Bi_2GdO_4Cl ratio is achieved with the specific ratio influencing both the crystal and electronic structures of the intergrowths. This compositional flexibility and crystal structure engineering can be leveraged for photocatalytic applications, with comparisons to the previously reported Bi_4TaO_8Cl–Bi_2GdO_4Cl intergrowth revealing how subtle structural and compositional features can impact photocatalytic materials.

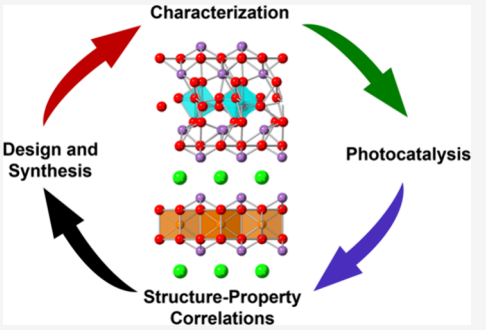

INTRODUCTION

Solar-driven photocatalytic processes play a crucial role in generating sustainable fuels and remediating pollutants.[1] Metal oxides like TiO_2 are benchmark photocatalytic materials.[2] However, metal oxides have wide band gaps, resulting in poor absorption of visible light.[3] In contrast, mixed anion materials such as metal oxynitrides,[4] oxysulfides,[5] and oxyhalides[6,7] that contain d^0 or d^{10} metal cations often have suitable band alignments for photocatalysis and appreciable visible-light absorption.[8] Despite these advantages, these mixed anion materials often lack photostability.[9] Photocorrosion can occur by oxidation of the nonoxide anions from holes generated in the valence band, as indicated here for chloride ions in oxychlorides ($2\ Cl^- + 2\ h^+ \rightarrow Cl_2$).[9] Furthermore, point defects in the crystal structure result in increased electron–hole recombination.[10]

Mixed metal oxyhalide materials such as Bi_4MO_8X (M = Nb and Ta; X = Cl and Br) and Bi_2AO_4X (A = La, Gd, Y; X = Cl, Br, and I) have gained attention due to suitable band alignment, minimal electron–hole recombination, and photostability.[9,11−13] Ogawa et al. synthesized Bi_4NbO_8Cl using a flux method, loaded RuO_2 as cocatalyst, and used the material for efficient Z-scheme water splitting under visible light, with an apparent quantum efficiency of 1.3% at 420 nm for O_2 evolution activity.[14] Similarly, Tao et al. have reported Bi_4TaO_8X (X = Cl, Br) microplatelets loaded with RuO_2 for photocatalytic water oxidation with an apparent quantum efficiency as high as 20% at 420 nm.[15] Nakada et al. reported Bi_2YO_4Cl for photocatalytic oxygen evolution at the rate of 13 μmol g^{-1} h^{-1} without a cocatalyst.[13] Loading a $(Fe,Ru)O_x$ cocatalyst on Bi_2YO_4Cl enhanced the rate of evolution of the O_2 by ∼7 times. Although these multimetal oxyhalides are visible-light absorbers and can facilitate photocatalytic reactions, the ability to tune the optoelectronic properties of these materials is limited.[16]

Recently, our group showed that intercalating layers of Bi_4TaO_8Cl and Bi_2GdO_4Cl to form intergrowths was possible and that the resulting structures were visible-light-absorbing materials with high photostability.[17] According to the revised lone pair model, Bi 6s electrons strongly interact with the O 2p orbitals in the valence band.[18] This interaction results in O 2p orbitals being the valence band maxima (VBM), curtailing photooxidation of the halide anions. The conduction band minima (CBM) for both Bi_4TaO_8Cl and Bi_2GdO_4Cl are composed of Bi 6p orbitals. Interestingly, for Bi_2GdO_4Cl, the

Received: January 23, 2024
Revised: March 27, 2024
Accepted: April 2, 2024
Published: April 19, 2024

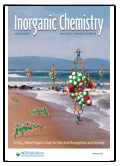

https://doi.org/10.1021/acs.inorgchem.4c00306
Inorg. Chem. 2024, 63, 8131–8141

$[GdO_2]^-$ layer inserted between two $[BiO]^+$ layers changes the symmetry around the Bi site, leading to changes in the position of CBM.[13] In addition, effective charge separation results from the internal static electric field generated by alternating layers of the intergrowths.

Here, the synthesis of intergrowth Bi_4NbO_8Cl–Bi_2GdO_4Cl is reported. This demonstration tests the generality of intergrowth formation as a pathway to metal oxyhalides with tunable optoelectronic properties and the hypothesis that both intergrowth stoichiometry and M identity serve as levers toward tunable photocatalytic performance. The crystal structures of Bi_4NbO_8Cl and Bi_2GdO_4Cl are shown in Figure 1, projected along their [110] (Figure 1a,b) and [001] (Figure 1d,e) directions, respectively. Bi_4NbO_8Cl is a Sillén–Aurivillius perovskite oxyhalide that has been reported to crystallize in the space group $P2_1cn$ (Figure 1c,f);[19] however, DFT calculations reported herein identify the space group $Pca2_1$ as energetically more favorable (Figure 1a,d). The unit cell of $Pca2_1$ is composed of the alternately charged layers of fluorite-type $[Bi_2O_2]^{2+}$, $[NbO_4]^{3-}$, and $[Cl]^-$. Bi_4NbO_8Cl can also be written as $[Bi_2O_2Cl]$ $[Bi_2NbO_6]$ where the Sillén and Aurivillius structures are separately denoted. Bi_2GdO_4Cl has alternating layers of triple fluorite-like $[Bi_2GdO_4]^+$ and $[Cl]^-$ exhibiting the centrosymmetric $P4/mmm$ space group, where the Gd is in a cubic coordination environment (Figure 1b,e). Our strategy involves intercalating layers of Bi_4NbO_8Cl and Bi_2GdO_4Cl along the c-directions of these materials, which correspond to the stacking direction of the layers described above. By systematically studying the Bi_4NbO_8Cl–Bi_2GdO_4Cl intergrowth system, we can identify how modulation of metal identity and stoichiometry results in variations in the structure and electrostatic destabilization of the atomic orbitals.

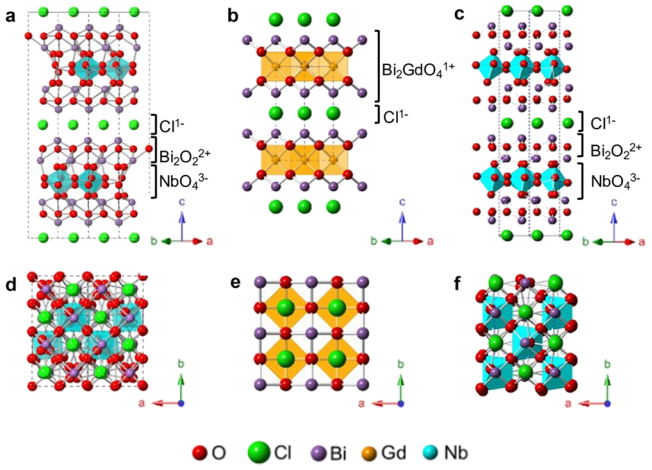

Figure 1. Crystal structures of (a, d) Bi_4NbO_8Cl ($Pca2_1$), (b, e) Bi_2GdO_4Cl ($P4/mmm$), and (c, f) Bi_4NbO_8Cl ($P2_1cn$) projected along their (a, b, c) [110] and (d, e, f) [001] directions, respectively.

Examination of the M–O–M (M = Nb, Gd) bond angles as a function of intergrowth stoichiometry is crucial to determining factors affecting the optoelectronic properties and photocatalytic performance of these materials. For instance, Kudo et al. correlated the photocatalytic activity of $Sr_2M_2O_7$ to the angle of O–M–O (M = Nb, Ta) bonds.[20] The more covalent bonding of Nb^{5+} compared to Ta^{5+} leads to the second-order Jahn–Teller distortion and energy stability gain.[21] Nb^{5+} shows an off-center displacement, whereas Ta^{5+} preferentially remains in a more centrosymmetric environment. As a result, the O–Ta–O bond angle in $Sr_2Ta_2O_7$ is close to 180°, leading to higher mobility of the photogenerated charge carriers; these features increase photocatalytic activity relative to $Sr_2Nb_2O_7$.[20,21] Likewise, as we report here, we can correlate the crystal and electronic structures of these intergrowths with photocatalytic performance to facilitate the design of new materials with tunable optoelectronic properties, addressing needs in the renewable energy sector and allied fields.

EXPERIMENTAL SECTION

Reagents. All chemicals were of reagent grade or higher and were used as received. Bismuth(III) oxide (Bi_2O_3, Sigma-Aldrich, 99.99%), niobium(V) oxide (Nb_2O_5, Sigma-Aldrich, 99.9%), bismuth chloride oxide (BiOCl, Alfa Aesar, 98%), gadolinium oxide (Gd_2O_3, Alfa Aesar, 99.9%), cesium chloride (CsCl, Sigma-Aldrich, 99.9%), iron(III) chloride hexahydrate ($FeCl_3{\cdot}6H_2O$, Sigma-Aldrich, ≥98%), hydrochloric acid (HCl, Fisher Chemical, ACS grade), ruthenium(III) chloride hydrate ($RuCl_3{\cdot}nH_2O$, Alfa Aesar, 99.99%), methanol (CH_3OH, Macron, ACS grade), absolute ethanol (C_2H_5OH, Macron, ACS grade), and acetone (C_3H_6O, Macron, ACS grade) were used as received without further purification. Nanopure water, having resistivity of 18.2 MΩ·cm at 25 °C, was used in all the syntheses and workup procedures.

Solid-State Synthesis of Bi_4NbO_8Cl and Bi_2GdO_4Cl. To obtain Bi_4NbO_8Cl, Bi_2O_3, Nb_2O_5, and BiOCl (with a molar ratio of 3:1:2) were used as precursors. For Bi_2GdO_4Cl, Bi_2O_3, Gd_2O_3, and BiOCl (with a molar ratio of 1:1:2) were used as precursors. Excess BiOCl was added to both syntheses to account for its volatility at elevated temperatures. The precursors were weighed and then crushed for 20 min using a mortar and pestle for homogeneous mixing. The fine powder containing the mixture of reagents was then added to an alumina crucible and transferred into a tube furnace, which was followed by heating to 800 °C at a ramp rate of 8.6 °C/min, under a N_2 gas flow of 20 mL/min, followed by calcination at 800 °C under a N_2 gas flow of 20 mL/min. To obtain Bi_4NbO_8Cl, 10 h of calcination was required whereas only 4 h was required for Bi_2GdO_4Cl. Products were cooled under a N_2 flow until room temperature was reached, pulverized, and stored for further characterization.

Optimized Flux Synthesis of the Bi_4NbO_8Cl–Bi_2GdO_4Cl Intergrowths. The procedure was similar to the solid-state synthesis described above with the addition of CsCl for flux formation. The flux was mixed at a solute concentration $[x/(x + y)$, where x is the total number of moles of precursors that will react to form the intergrowth and y is the number of moles of CsCl salt] of 5 mol %. The optimized set of reaction parameters is shown in Table S1. Once the reaction was completed, the flux salt was removed from the product by dispersing the sample in distilled water and then collecting the solids by centrifugation; this washing procedure was completed with distilled water three times followed by ethanol once. Products were dried under a vacuum overnight, pulverized, and stored for further characterization.

Materials Characterization. Powder X-ray diffraction (PXRD) data was collected using a PANalytical Empyrean diffractometer provisioned with a Cu source ($K\alpha_1$ radiation, λ = 1.5418 Å) and an X'Celerator linear strip detector operating at 45 kV and 40 mA. The fine powder obtained by grinding the solid samples was placed on a zero background Si sample holder, which was spun at the rate of 2 rev/min. The measurements ranged from 5 to 80° 2θ with a scan speed of 1.25°/min with 0.017° step size.

Field-emission scanning electron microscopy (FESEM) of samples was performed on an FEI Quanta 600F operated at 30 kV. Energy-dispersive X-ray spectroscopy (EDS) used an Oxford INCA detector interfaced to the FESEM. SEM was also conducted with a Zeiss Auriga 60 operated at 30 kV, along with an Oxford INCA detector for EDS analysis. To prepare samples for these analyses, approximately 1 mg of the solid sample was dispersed in a few drops of ethanol. A small piece of silicon wafer was attached to the alumina stage using carbon tape, and 2–5 μL of the dispersion was drop-casted onto the

https://doi.org/10.1021/acs.inorgchem.4c00306
Inorg. Chem. 2024, 63, 8131–8141

silicon wafer. The sample was dried under atmospheric conditions for 15 min before imaging.

Scanning transmission electron microscopy (STEM) images were collected on a JEOL JEM 3200FS operating at 300 kV using a Gatan 4K × 4K Ultrascan 4000 camera along with an Oxford INCA detector for EDS mapping. Samples for STEM analysis were prepared by drop-casting 2 μL of a dispersed particle solution onto a 300-mesh carbon-coated copper grid and allowed to dry under atmospheric conditions.

For high-resolution STEM, powder samples were dispersed in ethanol and drop-cast onto ultrathin carbon-coated Mo grids. STEM imaging was performed with an aberration corrected JEOL ARM200CF operated at 200 kV. The convergence semiangle for imaging was set to 27.51 mrad using a 40 μm condenser aperture, which gives a probe current of about 23 pA. The collection semiangle ranges for HAADF and ABF are 90−370 and 10−23 mrad, respectively. Micrographs were acquired at an electron probe size of 8C (JEOL defined), which are measured to be around 1.28 Å, and a pixel dwell time of 10 μs. Surface area measurements were calculated from N_2 isotherms using a Micromeritics ASAP 2020 analyzer according to standard eight-point Brunauer−Emmett−Teller (BET) analysis techniques. Before data collection, the samples were vacuum degassed at 120 °C (ramp rate of 1 K/min) overnight.

Diffuse reflectance spectroscopy (DRS) was conducted on a Varian Cary 100 Bio UV−visible spectrophotometer equipped with a Cary 301 DR accessory. The powder sample was loaded and pressed onto a cylindrical powder holder with dimensions of 3 mm height × 17 mm diameter. $BaSO_4$ was used as the 100% reflectance reference.

X-ray photoelectron spectroscopy (XPS) of samples was performed using a PHI 5000 Versa Probe II scanning X-ray microprobe under ultrahigh-vacuum conditions with a monochromatic Al Kα X-ray source. A beam size of about 200 μm and an X-ray power of 50 W at 15 keV under ultrahigh vacuum (UHV) conditions were used for all experiments. The binding energy of the C 1s peak was calibrated using the standard value (284.3 eV) of highly ordered pyrolytic graphite (HOPG).[22] Although resolution of VBM energy levels obtained using ultraviolet photoelectron spectroscopy (100−200 meV) is better than that of XPS (500 meV),[23] the latter was used as the samples were not conductive enough to avoid charge buildup due to the ejected electrons, resulting in generation of electric fields that can affect the kinetic energies and trajectories of the low energy electrons.[23]

X-ray total scattering (TS) data of the samples were collected at DanMAX,[24] the diffraction beamline at the MAX IV Laboratory (Lund, Sweden). TS data were collected for 60 s with an X-ray energy of 35 keV by using a Dectris PILATUS3 X CdTe 2 M area detector. The sample-to-detector distance was set to 100 mm. The samples were loaded in Ø1 mm Kapton capillaries, and the signal measured from an empty capillary was used for background subtraction. The 2D detector images were integrated using the pyFAI package using the Dioptas program.[25,26] PDFs were obtained from the TS data using the xPDFSuite software,[27] setting $Q_{max\text{-}inst}$ to 20.2 Å^{-1}, Q_{max} to 20.0 Å^{-1}, Q_{min} to 0.5 Å^{-1}, and r-poly to 0.9 Å. Real-space Rietveld refinement refinements were conducted using TOPAS.[28] Instrumental parameters (Q_{damp} = 0.0347 Å^{-1} and Q_{broad} = 0.0001 Å^{-1}) were refined from a LaB_6 standard.

Electronic Structure Studies. We perform first-principles density functional calculations within the Perdew−Burke−Ernzerhof approximation (PBE)[29] as implemented in the Vienna *Ab initio* Simulation Package (VASP)[30,31] with the projector augmented wave (PAW) method[32] to treat the core and valence electrons using the following electronic configurations $5d^{10}6s^26p^3$ (Bi), $4p^64d^45s^1$ (Nb), $5p^66s^25d^1$ (Gd), $3s^23p^5$ (Cl), $2s^22p^4$ (O), and a 500 eV plane wave cutoff. Note that f semicore electrons of Gd are treated as core states despite being higher in energy than other valence states. All structures are fully relaxed (forces to be less than 0.1 meV A^{-1}) with Gaussian smearing (0.02 eV width) for the Brillouin zone (BZ) integrations. For the group theoretical analysis, we use the AMPLIMODES software.[33,34] Due to the origin ambiguity in polar structures, we choose the origin of the low-symmetry structure so that the arithmetic center remains fixed when mapping the high-symmetry structure onto the low-symmetry phase. In all calculations, the influence of magnetism is not taken into consideration. This is attributed to Nb being in the 5+ valence state, resulting in a d^0 electronic configuration.

Photocatalytic Measurements. Photocatalytic OER and HER analyses were conducted in the liquid phase (Figure S1). For photocatalytic OER experiments, 15 mg of photocatalyst was dispersed in 10 mL of aqueous $FeCl_3$ (5 mM) solution. In the presence of $FeCl_3$ as an electron scavenger, the pH of the solution was lowered to ∼2.4 with dilute HCl to prevent $Fe(OH)_3$ precipitation. For photocatalytic HER experiments, 15 mg of photocatalyst was dispersed in 10 mL of aqueous methanol solution. Initially, 10 vol % of aqueous methanol was screened for photocatalytic HER. Due to low H_2 evolution, the amount of methanol was elevated to 20 vol % to increase the concentration of the hole scavenger to facilitate the reaction. These solutions were contained in a 24 mL quartz test tube reactor. The reactor was vacuum-treated and backfilled with helium (OER) or argon (HER) gas three times. The photocatalytic OER activity was evaluated for 4 h under full arc irradiation of a xenon lamp (Newport 66902, 300 W) and an attached water filter to avoid near-IR radiation above 850 nm. An additional 400 nm cut-on filter was used for photocatalytic HER. At regular time intervals, 500 μL of gas was manually removed through a gas septum using a syringe and the aliquot was analyzed using a GC (Agilent 6890N) equipped with the thermal conductivity detector (TCD).

Quantum Yield Measurements. The apparent quantum efficiency (AQE) was estimated from the following equations:[35]

$$\text{AQE of HER} = 2 \times \frac{\text{number of } H_2 \text{ molecules evolved}}{\text{total number of photons absorbed}} \times 100\%$$

$$\text{AQE of OER} = 4 \times \frac{\text{number of } O_2 \text{ molecules evolved}}{\text{total number of photons absorbed}} \times 100\%$$

$$\text{total number of photons absorbed} = \frac{\text{light absorbed by the photocatalyst}}{\text{energy of the photon}} \times \text{time}$$

$$\text{light absorbed by the photocatalyst} = \text{irradiance} \times \text{area of the reactor}$$

$$\text{energy of the photon} = \frac{hc}{\lambda}$$

The gas evolution rate was determined from the first hour of light irradiation. Average photon flux was estimated using a power meter to obtain ∼184 and 164 mW cm^{-2} for full arc and ≥400 nm wavelength for Xe lamp irradiation, respectively. The average wavelength (λ) of the broadband light source was estimated with reference to the band gap of the photocatalyst, as the irradiation of photons with energy greater than or equal to band gap energy results in the generation of photoexcited electron−hole pairs.[35]

RESULTS AND DISCUSSION

The Bi_4NbO_8Cl−Bi_2GdO_4Cl intergrowths were prepared by using a molten flux method. Nb_2O_5 and Gd_2O_3 were used as Nb and Gd sources, respectively, with both Bi_2O_3 and BiOCl contributing to the Bi stoichiometry. BiOCl and alkali halide flux are sources of halide ions. These oxide and oxyhalide precursors were chosen because (i) they do not have additional elements that can introduce impurities or result in competing phases and (ii) molten flux syntheses have been reported for Bi_4NbO_8Cl and Bi_2GdO_4Cl with the mentioned precursors.[9,14] BiOCl is volatile at the synthesis conditions, having a boiling point of 461 °C,[36] whereas the synthesis occurs at 700 °C. BiOCl was added to the reaction at greater than stoichiometric amounts to account for its volatility.[14] A variety of chloride fluxes and heating conditions were screened for the proposed

https://doi.org/10.1021/acs.inorgchem.4c00306
Inorg. Chem. 2024, 63, 8131−8141

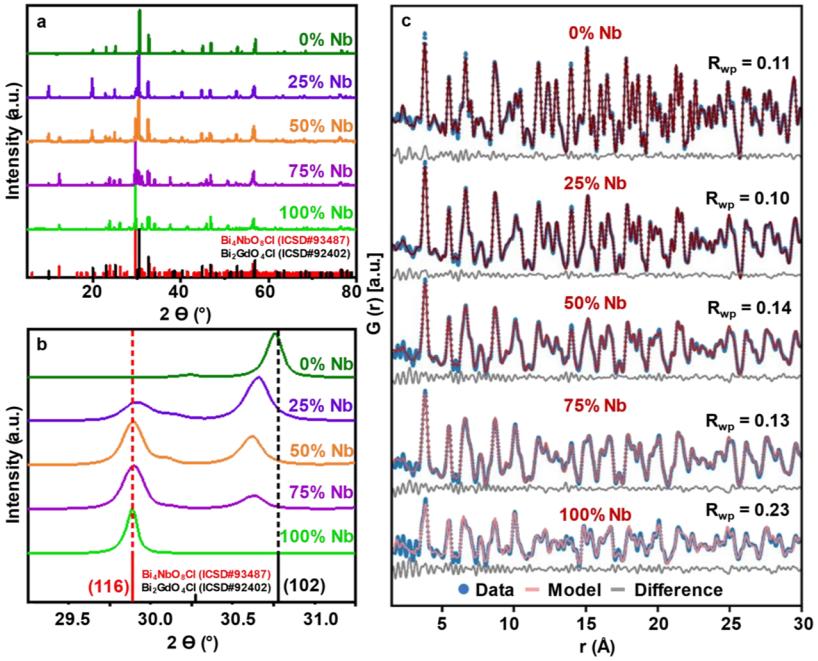

Figure 2. (a) PXRD patterns of samples in 2θ range from 5 to 80°. (b) Enlarged PXRD pattern centered around 2θ = 30°. (c) Real-space Rietveld refinement of end members and intergrowths' PDF. Blue dots, red trace, and ash trace correspond to the data, model, and difference between the data and model, respectively.

Bi_4NbO_8Cl–Bi_2GdO_4Cl intergrowths, with CsCl at 700 °C for 12 h being determined to be the most suitable based on producing the product of homogeneous morphology, i.e., plate-like particles (Figure S2) and achievement of targeted stoichiometry by SEM-EDS. Intergrowths with different ratios of Bi_4NbO_8Cl-to-Bi_2GdO_4Cl were targeted by varying the ratio of precursors in the syntheses (Table S1). The products will be referred to as 75% Nb, 50% Nb, and 25% Nb intergrowths, although slight deviations from ideal stoichiometry are noted (Table S2). The dissolution of niobium oxide in the molten salt during the synthesis results in the formation of volatile niobium oxychloride species, resulting in a slightly lower percentage of Nb than the ideal stoichiometry.[37,38] The parent Bi_4NbO_8Cl and Bi_2GdO_4Cl phases were synthesized for comparison using solid-state heating of the appropriate precursors (Figure S2 and Table S1). Brunauer–Emmett–Teller (BET) analysis on the parent compounds did not yield reliable specific surface areas due to the large agglomerates (being <1 m^2/g), but the specific surface areas of 75% Nb, 50% Nb, and 25% Nb intergrowth materials were slightly higher at 1.4, 2.6, and 1.6 m^2/g, respectively.

PXRD shows that the Bi_4NbO_8Cl and Bi_2GdO_4Cl structures were obtained in sample 100% Nb and 0% Nb, respectively (Figure 2a). PXRD patterns also support the formation of intergrowths. For the intergrowths, shifts toward lower diffraction angles are evident for reflections corresponding to the Bi_2GdO_4Cl phase of the intergrowth (Figure 2b), indicating an increase in d-spacing relative to the parent Bi_2GdO_4Cl phase. Interestingly, reflections ascribed to Bi_4NbO_8Cl do not exhibit any obvious shifts.

Bi_2GdO_4Cl possesses an ideal tetragonal centrosymmetric crystal structure with $P4/mmm$ symmetry.[39] The structure obtained through DFT relaxation closely matches the experimental structure with a mere 1.5% reduction in volume. Bi_4NbO_8Cl is cited as a Sillén–Aurivillius perovskite oxyhalide with space group $P2_1cn$.[19] In spite of that, DFT indicates that the $P2_1cn$ phase is unstable and spontaneously relaxes into a structure in the centrosymmetric $Pbcn$ space group. Similar outcomes were observed when van der Waals corrections were taken into account (data not included). Therefore, in the following, we do not consider van der Waals corrections. To check the dynamic stability of the $Pbcn$ phase, first-principles Γ-point phonon calculations were performed. We found that this structure is unstable at low temperatures and can transform to either the polar orthorhombic $Pca2_1$ polymorph or the centrosymmetric monoclinic $P2_1/c$ polymorph, which is essentially energetically degenerate. All DFT structure solutions are given in the Supporting Information as CIF files.

As described previously with the Bi_4TaO_8Cl–Bi_2GdO_4Cl system, intergrowth formation gives rise to distortions of the crystal structure, which are from the idealized model. To gain more insights into this effect, PDF analysis was performed on the TS data for the end members and intergrowth samples (Figure 2c). Even though both $Pca2_1$ and $P2_1/c$ polymorphs exhibit good agreement with the real-space Rietveld refinement of the PDF data of the 100 and 50% Nb samples, the $Pca2_1$ polymorph yields slightly better fits (Figure S3 and Tables S3 and S4). Structural refinement of the PDF data was performed using a simple two-phase model consisting of the two end-member phases (the $Pca2_1$ cell determined by DFT calculation for Bi_4NbO_8Cl and CIF no. 92402 from the ICSD database for Bi_2GdO_4Cl), where the selected r-range remains within that of one-unit cell for these systems and allows us to refine the two parent structures independently.[39] During the refinements, the cell parameters, Bi and Nb atomic coordinates, their atomic displacement parameters (ADPs) as well as those of Gd, O, and Cl, and the scaling factor and phase fraction of each parent structure were refined. All information about the refinement of samples Nb 100, 75, 50, 25, and 0% are summarized in Tables S3–S7, respectively.

The atomic percentage of Nb with respect to Gd was estimated based on the refined weight fraction of parent

https://doi.org/10.1021/acs.inorgchem.4c00306
Inorg. Chem. 2024, 63, 8131–8141

Table 1. Real-Space Rietveld Refinement of Pristine and Intergrowth Samples, Indicating the Evolution in the *a*, *b*, and *c* Lattice Parameters

sample	a-axis Nb [Å]		b-axis Nb [Å]		c-axis Nb [Å]		a-axis Gd [Å]		c-axis Gd [Å]	
		percentage difference from 100% Nb		percentage difference from 100% Nb		percentage difference from 100% Nb		percentage difference from 0% Nb		percentage difference from 0% Nb
100% Nb	5.449	0%	5.492	0%	28.634	0%				
75% Nb	5.452	0.06%	5.496	0.07%	28.673	0.14%	3.882	0.28%	8.967	0.56%
50% Nb	5.453	0.07%	5.493	0.02%	28.672	0.13%	3.884	0.34%	8.958	0.46%
25% Nb	5.45	0.02%	5.491	0.02%	28.669	0.12%	3.883	0.31%	8.946	0.32%
0% Nb							3.871	0%	8.917	0%

structures. As shown in Figure S4, this agrees with the SEM-EDS data. Good agreement between the experimental data and the two-phase models was obtained from real-space Rietveld refinements, as indicated by the weighted-pattern agreement factor (R_{wp}) values (Figure 2c). Lattice parameters were extracted by refinement to investigate the structure variations upon intergrowth formation. As shown in Table 1, the *c* parameters corresponding to the stacking directions of both Bi_2GdO_4Cl and Bi_4NbO_8Cl increase as intergrowth formation takes place. The Gd phase expands also in the (*a*,*b*) plane with addition of the Nb phase from intergrowth formation, but little change is evident for the Nb phase. These observations are consistent with the PXRD changes upon intergrowth formation (Figure 2b).

Further, the O−Nb−O and Gd−O−Gd bond angles were extracted from the refined structures of the PDF analysis and are summarized in Table 2. We observe the axial O−Nb−O bond angles along the *c* direction and basal O−Nb−O angles in the (*a*,*b*) plane diverging from the end member samples, whereas Gd−O−Gd bond angles show minimal changes upon intergrowth formation (Table 2). The 100 and 75% Nb samples have the axial O−Nb−O angle closest to 180°, namely, 169 and 170°, while for lower Nb% samples, this angle is becoming smaller, 166 and 164° in 50 and 25% Nb, respectively. These observations suggest a gradual loss of centrosymmetry of the [NbO_6] octahedra as the Nb% decreases. Simultaneously, the basal O−Nb−O angle, in the Nb-rich samples, is the closest to 90°, i.e., an "ideal" centrosymmetric [NbO_6] unit, 105.0 and 104.3° for samples Nb 100 and 75%, respectively, while for the two other samples, it is 108.9 and 111.3°. Recall that mobility of photogenerated charge carriers is anticipated to be greatest when the bond angle is closest to 180°.

Table 2. Metal−O−Metal Bond Angle for the Different Samples

sample	axial O−Nb−O angle [°]	basal O−Nb−O angle [°]	Gd−O−Gd angle [°]
100% Nb	169	105.0	
75% Nb	170	104.3	108.09
50% Nb	166	108.9	108.18
25% Nb	164	111.3	108.24
0% Nb			108.25
ideal	180	90	109.45

In addition, XPS probed the oxidation states of the elements in the 50% Nb intergrowth, with Bi, Nb, Gd, Cl, and O evident in the survey scan (Figure S5a). High-resolution spectra of the Bi 4f, Nb 3d, Gd 4d, O 1s, and Cl 2p regions show anticipated features as described in the SI (Figure S5b−f). STEM-EDS elemental mapping shown in Figure S6 of the intergrowths indicates a homogeneous distribution of elements at the nanoscale throughout individual particles.

To further investigate the structure of the intergrowths at the atomic level, the 50% Nb intergrowth was analyzed by aberration-corrected scanning transmission electron microscopy (ac-STEM). Annular dark-field (ADF) images and bright-field (BF) images were captured along the ⟨001⟩ and ⟨110⟩ zone axes. The view along ⟨001⟩ (Figure 3a,b) exhibits the expected squared pseudocubic lattice, the A-type sites are expected to be occupied by Bi, Nb, or Gd while B-type sites are occupied by Bi and Cl. In addition, the view along ⟨110⟩ (Figure 3c,d) depicts the layered structure. These high-resolution micrographs help us to conclude that no apparent atomic segregation of Nb−Gd occurs in the 50% mixing.

DRS of the intergrowths shows onsets of absorption from 700 nm, with sharp absorption edges around ∼480 nm, indicating the capability of these materials to absorb visible light (Figure 4a). The slight tailing effect in the exponential region is known as Urbach tailing and arises from the cumulative effect of structural disorders such as defects and doping.[40,41] Bandgap energies were determined by Tauc plots (Figure S7), generated using the Kubelka−Munk function (indirect band gaps).[42] The band gap is measured as the intercept of the slope at the leading edge of the Kubelka−Munk plot with its baseline. The Urbach tailing limits accurate determination of the band gap as the exponential region of the curve is less steep for the intergrowths compared to the end members. Bi_4NbO_8Cl and Bi_2GdO_4Cl have band gaps of 2.41 and 2.34 eV, respectively, whereas the intergrowths 25, 50, and 75% Nb have band gaps of 2.26, 2.24, and 2.38 eV, respectively. A plot of bandgap energy as a function of Nb% is provided in the inset of Figure 4a and compared to the parent compounds, giving a U-shape plot. That is, the 50% Nb sample has the smallest band gap.

However, visible-light absorption is only one of the important features for an effective photocatalyst. Also, the conduction and valence bands must straddle the redox potentials of the oxidation and reduction processes of interest. The band gaps obtained from DRS combined with the VBM estimated by using XPS provide the band structure of the materials.[43] The band alignments are schematically represented in Figure 4b, with the standard reduction potentials for the OER and HER relative to the normal hydrogen electrode (NHE) at pH = 0 also indicated. The CBMs and VBMs satisfy the thermodynamic conditions for water splitting.

To obtain further insights into the electronic structure of the layered structures, DFT calculations were performed on the end members and the *Pc* intergrowth model of the 50% Nb sample (see the provided CIF files). Figure S8 shows the

https://doi.org/10.1021/acs.inorgchem.4c00306
Inorg. Chem. 2024, 63, 8131−8141

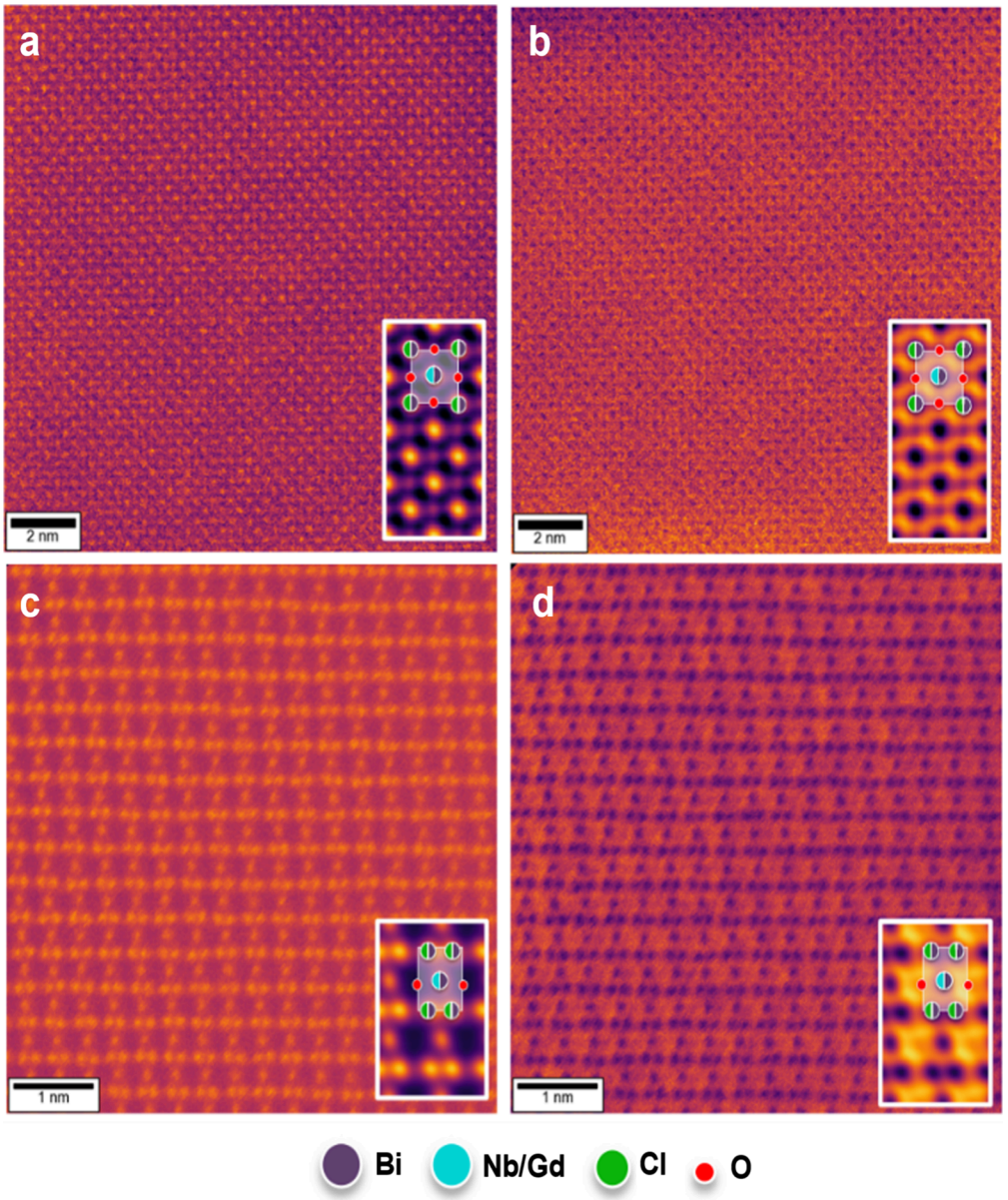

Figure 3. Microstructural analysis of the 50% Nb sample was performed using STEM. (a) ADF image viewed along the <001> axis showing typical perovskite pseudocubic lattice while (b) shows simultaneously acquired ABF image. Insets in (a) and (b) presents an averaged unit. (c) and (d) show ADF and ABF images, respectively, viewed along the <110>. Insets in (c) and (d) present an averaged unit cell overlaid with the 50% Nb structure.

electronic band structure as a function of the Nb concentration. The computed optical band gaps from the electronic band structure are 1.49, 1.43, and 1.55 eV for the 0, 50, and 100% Nb samples, respectively. These values exhibit good agreement with the optical absorption calculated by using DFT (see Figure S9), aligning qualitatively with the trend derived from DRS. That is, while DFT calculations generally underestimate the experimental band gap,[44] the U-shape trend of the DFT optical band gaps upon chemical substitution (Figure S10) is consistent with the experimental measurement (Figure 4a). Note that introducing the parameter *U* to reproduce the experimentally observed band gap would result in a fit of the data and, of course, align with the correct experimental trend; however, such an adjustment would be an artifact of the methodology.

Figure 4c shows the projected density of states (DOS) as a function of the Nb concentration. In all cases, the Cl 3p states are strongly localized and located approximately 2 eV below the valence band edge (VBE) within a broad O 2p band. In both end members, the conduction band edge (CBE) is composed largely of Bi 6p states, with Nb 4d states in the case of Bi_4NbO_8Cl. The DOS of the 50% Nb compound can be described as a direct superposition of the two end members, which indicates that the layers are largely decoupled from one another. In the CBE, the dominance of Bi 6p states is evident, while in the VBE, O 2p states exert significant influence. Analysis of the projected DOS highlights a direct correlation between the U-shaped bandgap pattern and the displacement of a prominent O peak within the valence band (refer to Figure S11). Specifically, this peak is observed to be positioned at 109, 9, and 260 meV below the VBE for the 0, 50, and 100% Nb

https://doi.org/10.1021/acs.inorgchem.4c00306
Inorg. Chem. 2024, 63, 8131−8141

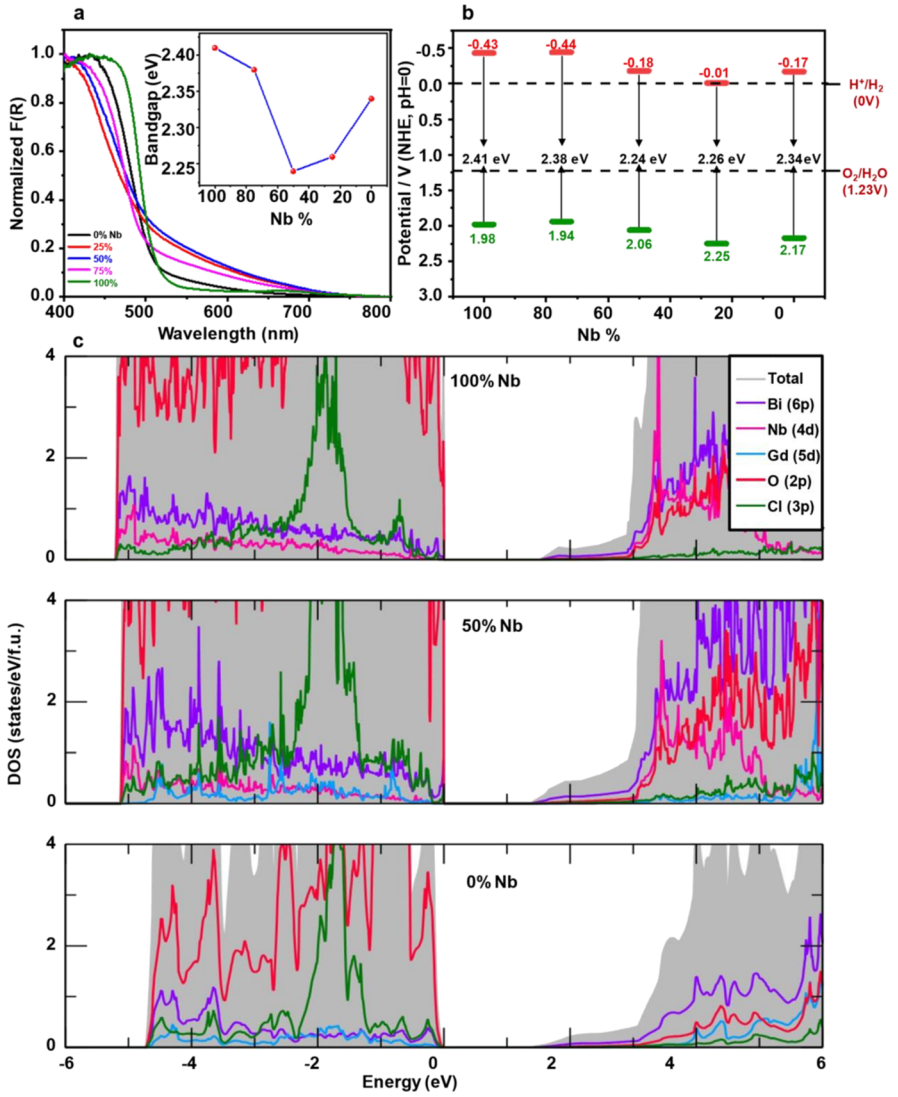

Figure 4. (a) Normalized Kubelka–Munk plots (bandgap trends in the inset). (b) Schematic representation of experimentally determined band alignments. (c) Projected density of states (DOS) of the 100, 50, and 0% Nb samples.

samples, respectively. Additionally, there is a minor contribution from the Bi 6p states hybridized with Cl 3p states (Figure S12).

The intergrowths were evaluated for the OER, resulting from water oxidation by holes generated near the VBM, as schematically shown in Figure S13. Figure S14a,b shows time courses of photocatalytic OER from the 0, 25, 50, 75, and 100% Nb samples in the presence of 5 mM of $FeCl_3$ as an electron scavenger. The AQE values were estimated to be 0.007, 0.01, 0.007, 0.02, and 0.01% for 0, 25, 50, 75, and 100%, Nb, respectively. All the photocatalysts show similar O_2 evolution rates, and the AQE values are significantly lower when compared to the previously reported Bi_4TaO_8Cl–Bi_2GdO_4Cl intergrowth system.[17] Similar amounts of O_2 evolution were observed for all photocatalysts after 1 h of irradiation when normalized to the mass of the sample, as shown in Figure S14b. The 50% Bi_4TaO_8Cl–Bi_2GdO_4Cl intergrowth exhibited remarkable OER activity with an AQE of 7.6% within the wavelength range of 400 to 500 nm with 1 wt % RuO_x as a cocatalyst.[17] The photocatalytic performance can be correlated to the crystal and electronic structures of photocatalysts, which will be discussed further shortly. Loading RuO_x as a cocatalyst led to a slight improvement in the OER (Figure S14c,d).

The intergrowths were also evaluated for the HER. Figure S15a,b shows time courses of photocatalytic HER with 0, 25, 50, 75, and 100% Nb samples in the presence of 20 vol % methanol as the hole scavenger. The AQE values were estimated to be 0.002, 0.002, 0.001, 0.002, and 0.001% for 0, 25, 50, 75, and 100% Nb, respectively. Although the intergrowths exhibited similar HER activity compared to the end members, a macroscopic color change from a yellow to black suspension was observed for all intergrowths upon irradiation in an argon atmosphere, in the presence of 20 vol % methanol (Figures S16 and S17). Interestingly, after the light source was turned off and the dispersion was exposed to air, the dispersion reverted to yellow. This color change, especially in comparison to the behavior of our previously studied Bi_4TaO_8Cl–Bi_2GdO_4Cl intergrowth, hints to the origin of the low photocatalytic activity; that is, such color changes are often associated with changes in metal oxidation states.[45]

XPS was used to examine the chemical states of the 50% Nb intergrowth immediately after the HER (4 h irradiation under argon), when the collected powder still appears gray rather

https://doi.org/10.1021/acs.inorgchem.4c00306
Inorg. Chem. 2024, 63, 8131–8141

than the initial yellow. As shown in Figure S18, the binding energies of Bi 4f, Cl 2p, and Nb 3d were unchanged with respect to the nonirradiated sample, implying negligible changes in their chemical states. However, differences were observed in the O 1s and Gd $3d_{5/2}$ regions. The Gd $3d_{5/2}$ peak shifted 0.18 eV toward higher binding energy. Also, the O 1s peak became more asymmetric and shifted 0.11 eV toward higher binding energy and a shoulder peak at 532.17 eV is shown, the latter of which corresponds to adsorbed oxygen species at the surface. The asymmetry of the O 1s has been commonly associated with oxygen vacancies;[46] however, a recent study by Frankcombe and Liu suggested that the peak cannot be directly correlated with oxygen vacancies.[47] Instead, the peak can be attributed to surface hydroxyls,[48−52] acting as a proxy for transient surface oxygen defects. The OH species generated by dissociative adsorption of water replace missing oxygen ions, whereas additional hydrogen species bind to other surface oxygens. While these vacancies were not directly observed, this designation is consistent with the color change back to yellow upon exposure to air, presumably from Gd sites adsorbing oxygen.

Similar to the Bi_4NbO_8Cl−Bi_2GdO_4Cl system, the 50% Bi_4TaO_8Cl−Bi_2GdO_4Cl intergrowth also produced very little H_2, which was attributed to its unsuitable conduction band position and unfavorable surfaces for proton adsorption.[17] However, a macroscopic color change was not observed during the HER experiments. Upon further examination of the projected DOS, insights into this macroscopic color change can be gained. In particular, there are differences in the contribution of Bi 6p and Nb 4d/Ta 5d states to the CBE (see Figures S19 and S20) when comparing the Bi_4NbO_8Cl−Bi_2GdO_4Cl and Bi_4TaO_8Cl−Bi_2GdO_4Cl intergrowths. In both cases, Bi 6p states dominate the CBE (Figure S19), accompanied by minor contributions from Nb 4d/Ta 5d and Gd 5d, as depicted in Figure S20. However, a smaller contribution of Ta 5d can be observed compared to Nb 4d states in the CBE. A similar trend is observed for the Gd 5d states as well. Based on this analysis, we conclude that the color changes observed in Bi_4NbO_8Cl−Bi_2GdO_4Cl intergrowths are from the larger contribution of Nb 4d and Gd 5d states compared to that of Ta 5d and Gd 5d states in Bi_4TaO_8Cl−Bi_2GdO_4Cl. Along with the possible contribution from point defects, the color change can be attributed to electron insertion into Nb 4d and Gd 5d orbitals near the CBE on photoexcitation, which would not be reflected in the XPS due to the very small amount of electrons.

The differences in the photocatalytic performance as a function of metal identity can be correlated with differences in defect states. Notably, the visible-light absorption (smaller band gap) and anticipated enhanced charge carrier mobility of the Bi_4NbO_8Cl−Bi_2GdO_4Cl intergrowths compared to the end members appear to be nullified by defects acting as charge carrier trapping and recombination sites. Annealing of the intergrowths did not reduce the Urbach tailing, indicating that these defects cannot be readily decreased (Figure S21 and the corresponding discussion). Thus, one interpretation is that changes in the crystal structure leads to the generation of point defects, influencing the photocatalytic performance.[53] The minimal distortion of $[NbO_6]$ octahedra upon intergrowth formation propels distortion of $[Bi_2GdO_4]$ instead to stabilize the crystal structure of the intergrowth (see Table 1). These distortions enable chemical changes under the reaction conditions for photocatalytic HER, with the point defects generated by distortions serving as the recombination sites of photogenerated charge carriers. However, in Bi_4TaO_8Cl−Bi_2GdO_4Cl intergrowth, distortion of $[TaO_6]$ octahedra preserves the structure of $[Bi_2GdO_4]$.[54] The distortion of $[TaO_6]$ octahedra leads to greater mobility of photogenerated electron−hole pairs, increasing the probability of the charge carriers to reach active sites on the surface of the photocatalyst and enhancing photocatalytic performance.

CONCLUSIONS

Bi_4NbO_8Cl−Bi_2GdO_4Cl intergrowths were synthesized via molten flux, with the stoichiometry being readily tuned by the input ratio of the precursors. Compositional homogeneity was evident from ac-STEM imaging, along with elemental mapping. The intergrowths have electronic structures capable of overall water splitting driven by visible light, with their VBM largely composed of O 2p orbitals to impart photostability. These features, coupled with the near-linear O−Nb−O bond angles, suggest that these intergrowths should be excellent photocatalysts; however, low activities for the OER and HER are reported even with cocatalysts. This finding contrasts with the Bi_4TaO_8Cl−Bi_2GdO_4Cl intergrowth system, emphasizing metal identity and composition as critical factors in regulating structure and point defects, influencing the photocatalytic performance and photostability of the multimetal oxyhalide intergrowths.

ASSOCIATED CONTENT

Supporting Information

The Supporting Information is available free of charge at https://pubs.acs.org/doi/10.1021/acs.inorgchem.4c00306.

Reaction conditions, simplified schematic of the reactor used for photocatalysis, additional characterization of intergrowths, data from PDF refinement, additional results from DFT calculations, photocatalysis, and results from control experiments (PDF)

DFT structure solutions (ZIP)

AUTHOR INFORMATION

Corresponding Author

Sara E. Skrabalak − *Department of Chemistry, Indiana University-Bloomington, Bloomington, Indiana 47405, United States;* orcid.org/0000-0002-1873-100X; Email: sskrabal@indiana.edu

Authors

Nayana Christudas Beena − *Department of Chemistry, Indiana University-Bloomington, Bloomington, Indiana 47405, United States;* orcid.org/0000-0001-9603-5475

Nicolas P. L. Magnard − *Department of Chemistry, University of Copenhagen, Copenhagen DK-2100, Denmark;* Present Address: Catalysis & Surface Chemistry (CASC), Leiden Institute of Chemistry (LIC), Leiden University, Einsteinweg 55, 2333 CC Leiden, The Netherlands

Danilo Puggioni − *Department of Materials Science and Engineering, Northwestern University, Evanston, Illinois 60208, United States;* orcid.org/0000-0002-2128-4191

Roberto dos Reis − *Department of Materials Science and Engineering and Northwestern University Atomic and Nanoscale Characterization Experimental (NUANCE) Center, Northwestern University, Evanston, Illinois 60208, United States*

https://doi.org/10.1021/acs.inorgchem.4c00306
Inorg. Chem. 2024, 63, 8131−8141

Kaustav Chatterjee − *Department of Chemistry, Indiana University-Bloomington, Bloomington, Indiana 47405, United States;* orcid.org/0000-0003-3527-9796
Xun Zhan − *Department of Chemistry, Indiana University-Bloomington, Bloomington, Indiana 47405, United States*
Vinayak P. Dravid − *Department of Materials Science and Engineering, Northwestern University Atomic and Nanoscale Characterization Experimental (NUANCE) Center, and International Institute of Nanotechnology, Northwestern University, Evanston, Illinois 60208, United States;* orcid.org/0000-0002-6007-3063
James M. Rondinelli − *Department of Materials Science and Engineering, Northwestern University, Evanston, Illinois 60208, United States;* orcid.org/0000-0003-0508-2175
Kirsten M. Ø. Jensen − *Department of Chemistry, University of Copenhagen, Copenhagen DK-2100, Denmark;* orcid.org/0000-0003-0291-217X

Complete contact information is available at: https://pubs.acs.org/10.1021/acs.inorgchem.4c00306

Author Contributions

N.C.B. and S.E.S. were responsible for the design of this project. N.C.B. synthesized the materials and performed structural, optical, and photocatalytic measurements. N.P.L.M. conducted synchrotron beamline experiments and real-space Rietveld refinements. D.P. performed the DFT calculations. R.d.R. acquired HAADF and ABF images. K.C. was responsible for XPS measurements. X.Z. performed STEM-EDS elemental mapping. N.C.B., N.P.L.M., D.P., and R.d.R. analyzed the results. N.C.B. and S.E.S. wrote the manuscript with input from all authors. V.P.D., J.M.R., K.M.Ø.J., and S.E.S. supervised the project.

Funding

This work was supported by Indiana University and US NSF DMR-2113536. K.M.Ø.J and N.P.L.M. gratefully acknowledge the Danish Ministry of Higher Education and Science for funding through the SMART Lighthouse. They further thank DANSCATT (supported by the Danish Agency for Science and Higher Education) for support. We acknowledge MAX IV Laboratory for the time on Beamline DanMAX. Research conducted at MAX IV is supported by the Swedish Research Council under contract 2018-07152, the Swedish Governmental Agency for Innovation Systems under contract 2018-04969, and Formas under contract 2019-02496. DanMAX is funded by the NUFI grant no. 4059-00009B. This work made use of the EPIC facility of Northwestern University's NUANCE Center, which has received support from the SHyNE Resource (NSF ECCS-2025633), the IIN, and Northwestern's MRSEC program (NSF DMR-1720139). Computational work at NU was supported by the NSF through DMR-2011208. Calculations were performed using the Department of Defense High-Performance Computing Modernization Program (DOD-HPCMP).

Notes

The authors declare no competing financial interest.

■ ACKNOWLEDGMENTS

We want to thank the IU Molecular Structure Center, Electron Microscopy Center, and Nanoscale Characterization Facility for access to the necessary instrumentation. We also want to thank Jaye K. Harada for preliminary calculations and Matthew N. Gordon, Yaroslav Losovyj, Zachary J. Woessner, Maha Ibrar, Amala Raj, and Yuda Li for the helpful discussions.

■ REFERENCES

(1) Balzani, V.; Pacchioni, G.; Prato, M.; Zecchina, A. Solar-Driven Chemistry: Towards New Catalytic Solutions for a Sustainable World. *Rend. Fis. Acc. Lincei* **2019**, *30* (3), 443−452.
(2) Jafari, T.; Moharreri, E.; Amin, A. S.; Miao, R.; Song, W.; Suib, S. L. Photocatalytic Water Splitting—The Untamed Dream: A Review of Recent Advances. *Molecules* **2016**, *21* (7), 900.
(3) Bakranov, N.; Zhabaikhanov, A.; Kudaibergenov, S.; Ibraev, N. Decoration of Wide Bandgap Semiconducting Materials for Enhancing Photoelectrochemical Efficiency of PEC Systems. *J. Phys.: Conf. Ser.* **2018**, *987*, No. 012028.
(4) Maeda, K. (Oxy)Nitrides with D^0-Electronic Configuration as photocatalysts and Photoanodes That Operate under a Wide Range of Visible Light for Overall Water Splitting. *Phys. Chem. Chem. Phys.* **2013**, *15* (26), 10537−10548.
(5) Takata, T.; Domen, K. Development of Non-Oxide Semiconductors as Light Harvesting Materials in Photocatalytic and Photoelectrochemical Water Splitting. *Dalton Trans.* **2017**, *46* (32), 10529−10544.
(6) Cheng, H.; Huang, B.; Dai, Y. Engineering BiOX (X = Cl, Br, I) Nanostructures for Highly Efficient Photocatalytic Applications. *Nanoscale* **2014**, *6* (4), 2009−2026.
(7) Gordon, M. N.; Chatterjee, K.; Christudas Beena, N.; Skrabalak, S. E. Sustainable Production of Layered Bismuth oxyhalides for Photocatalytic H2 Production. *ACS Sustainable Chem. Eng.* **2022**, *10* (48), 15622−15641.
(8) Maeda, K.; Takeiri, F.; Kobayashi, G.; Matsuishi, S.; Ogino, H.; Ida, S.; Mori, T.; Uchimoto, Y.; Tanabe, S.; Hasegawa, T.; Imanaka, N.; Kageyama, H. Recent Progress on Mixed-Anion Materials for Energy Applications. *BCSJ.* **2022**, *95*, 26.
(9) Kato, D.; Hongo, K.; Maezono, R.; Higashi, M.; Kunioku, H.; Yabuuchi, M.; Suzuki, H.; Okajima, H.; Zhong, C.; Nakano, K.; Abe, R.; Kageyama, H. Valence Band Engineering of Layered Bismuth oxyhalides toward Stable Visible-Light Water Splitting: Madelung Site Potential Analysis. *J. Am. Chem. Soc.* **2017**, *139* (51), 18725−18731.
(10) Shockley, W.; Read, W. T. Statistics of the Recombinations of Holes and Electrons. *Phys. Rev.* **1952**, *87* (5), 835−842.
(11) Bhat, S. S. M.; Swain, D.; Feygenson, M.; Neuefeind, J. C.; Mishra, A. K.; Hodala, J. L.; Narayana, C.; Shanbhag, G. V.; Sundaram, N. G. Bi_4TaO_8Cl Nano-photocatalyst: Influence of Local, Average, and Band Structure. *Inorg. Chem.* **2017**, *56* (10), 5525−5536.
(12) Fujito, H.; Kunioku, H.; Kato, D.; Suzuki, H.; Higashi, M.; Kageyama, H.; Abe, R. Layered Perovskite oxychloride Bi_4NbO_8Cl: A Stable Visible Light Responsive photocatalyst for Water Splitting. *J. Am. Chem. Soc.* **2016**, *138* (7), 2082−2085.
(13) Nakada, A.; Kato, D.; Nelson, R.; Takahira, H.; Yabuuchi, M.; Higashi, M.; Suzuki, H.; Kirsanova, M.; Kakudou, N.; Tassel, C.; Yamamoto, T.; Brown, C. M.; Dronskowski, R.; Saeki, A.; Abakumov, A.; Kageyama, H.; Abe, R. Conduction Band Control of oxyhalides with a Triple-Fluorite Layer for Visible Light Photocatalysis. *J. Am. Chem. Soc.* **2021**, *143* (6), 2491−2499.
(14) Ogawa, K.; Nakada, A.; Suzuki, H.; Tomita, O.; Higashi, M.; Saeki, A.; Kageyama, H.; Abe, R. Flux Synthesis of Layered Oxyhalide Bi_4NbO_8Cl photocatalyst for Efficient Z-Scheme Water Splitting Under Visible Light. *ACS Appl. Mater. Interfaces* **2019**, *11* (6), 5642−5650.
(15) Tao, X.; Zhao, Y.; Mu, L.; Wang, S.; Li, R.; Li, C. Bismuth Tantalum Oxyhalogen: A Promising Candidate photocatalyst for Solar Water Splitting. *Adv. Energy Mater.* **2018**, *8* (1), 1701392.
(16) Zhou, X.; Dong, H. Density Functional Studies on Layered Perovskite Oxyhalide Bi_4MO_8X photocatalysts (M = Nb and Ta, X = Cl, Br, and I). *J. Phys. Chem. C* **2017**, *121* (38), 20662−20672.
(17) Chatterjee, K.; Dos Reis, R.; Harada, J. K.; Mathiesen, J. K.; Bueno, S. L. A.; Jensen, K. M. Ø.; Rondinelli, J. M.; Dravid, V.; Skrabalak, S. E. Durable multimetal oxychloride Intergrowths for

Visible Light-Driven Water Splitting. *Chem. Mater.* **2021**, *33* (1), 347−358.
(18) Walsh, A.; Payne, D. J.; Egdell, R. G.; Watson, G. W. Stereochemistry of Post-Transition Metal Oxides: Revision of the Classical Lone Pair Model. *Chem. Soc. Rev.* **2011**, *40* (9), 4455−4463.
(19) Kusainova, A. M.; Stefanovich, S. Y.; Dolgikh, V. A.; Mosunov, A. V.; Hervoches, C. H.; Lightfoot, P. Dielectric Properties and Structure of Bi_4NbO_8Cl and Bi_4TaO_8Cl. *J. Mater. Chem.* **2001**, *11* (4), 1141−1145.
(20) Kudo, A.; Kato, H.; Nakagawa, S. Water Splitting into H_2 and O_2 on New $Sr_2M_2O_7$ (M = Nb and Ta) photocatalysts with Layered Perovskite Structures: Factors Affecting the Photocatalytic Activity. *J. Phys. Chem. B* **2000**, *104* (3), 571−575.
(21) Lufaso, M. W. Crystal Structures, Modeling, and Dielectric Property Relationships of 2:1 Ordered $Ba_3MM'_2O_9$ (M = Mg, Ni, Zn; M′ = Nb, Ta) Perovskites. *Chem. Mater.* **2004**, *16* (11), 2148−2156.
(22) Morales, C.; Díaz-Fernández, D.; Prieto, P.; Lu, Y. H.; Kersell, H.; Campo, A. del; Escudero, C.; Pérez-Dieste, V.; Ashby, P.; Méndez, J.; Soriano, L. In-Situ Study of the Carbon Gasification Reaction of Highly Oriented pyrolytic Graphite Promoted by Cobalt Oxides and the Novel Nanostructures Appeared after Reaction. *Carbon* **2020**, *158*, 588−597.
(23) Whitten, J. E. Ultraviolet Photoelectron Spectroscopy: Practical Aspects and Best Practices. *Appl. Surf. Sci. Adv.* **2023**, *13*, No. 100384.
(24) Jørgensen, M. R. V.; Sørensen, D. R.; Kantor, I.; Oller, S. F. DanMAX − the new materials science beamline at MAX IV. *Acta Crystallogr., Sect. A: Found. Adv.* **2021**, *77*, C821.
(25) Kieffer, J.; Valls, V.; Blanc, N.; Hennig, C. New Tools for Calibrating Diffraction Setups. *J. Synchrotron Rad.* **2020**, *27* (2), 558−566.
(26) Prescher, C.; Prakapenka, V. B. Dioptas: A Program for Reduction of Two-Dimensional X-Ray Diffraction Data and Data Exploration. *High Pressure Research* **2015**, *35* (3), 223−230.
(27) Yang, X.; Juhas, P.; Farrow, C. L.; Billinge, S. J. L. xPDFsuite: An End-to-End Software Solution for High Throughput Pair Distribution Function Transformation, Visualization and Analysis.*arXiv preprint arXiv:1402.3163***2014**
(28) Coelho, A. A. TOPAS and TOPAS-Academic: An Optimization Program Integrating Computer Algebra and Crystallographic Objects Written in C++. *J. Appl. Crystallogr.* **2018**, *51* (1), 210−218.
(29) Perdew, J. P.; Burke, K.; Ernzerhof, M. Generalized Gradient Approximation Made Simple. *Phys. Rev. Lett.* **1996**, *77* (18), 3865−3868.
(30) Kresse, G.; Furthmüller, J. Efficient Iterative Schemes for Ab Initio Total-Energy Calculations Using a Plane-Wave Basis Set. *Phys. Rev. B* **1996**, *54* (16), 11169−11186.
(31) Kresse, G.; Joubert, D. From Ultrasoft Pseudopotentials to the Projector Augmented-Wave Method. *Phys. Rev. B* **1999**, *59* (3), 1758−1775.
(32) Blöchl, P. E. Projector Augmented-Wave Method. *Phys. Rev. B* **1994**, *50* (24), 17953−17979.
(33) Orobengoa, D.; Capillas, C.; Aroyo, M. I.; Perez-Mato, J. M. AMPLIMODES: Symmetry-Mode Analysis on the Bilbao Crystallographic Server. *J. Appl. Crystallogr.* **2009**, *42* (5), 820−833.
(34) Perez-Mato, J. M.; Orobengoa, D.; Aroyo, M. I. Mode Crystallography of Distorted Structures. *Acta Cryst. A* **2010**, *66* (5), 558−590.
(35) Zubair, M.; Svenum, I.-H.; Rønning, M.; Yang, J. Core-Shell Nanostructures of Graphene-Wrapped CdS Nanoparticles and TiO_2 (CdS@G@TiO_2): The Role of Graphene in Enhanced Photocatalytic H_2 Generation. *Catalysts* **2020**, *10* (4), 358.
(36) Feng, S.; Xu, L.; Liu, C.; Du, H.; Xie, T.; Zhu, Q. Preparation and property of magnetic photocatalyst BiOCl/$Mn_xZn_{1-x}Fe_2O_4$. *J. Nanopart. Res.* **2017**, *19* (2), 33.
(37) Polovov, I. B.; Brevnova, N. P.; Volkovich, V. A.; Chernyshov, M. V.; Vasin, B. D.; Rebrin, O. I. Speciation of Niobium in Chloride Melts: An Electronic Absorption Spectroscopic Study. In *Molten Salts Chemistry and Technology*; John Wiley & Sons, Ltd, 2014; pp 243−255.
(38) Wang, H.; Huang, X.; Lin, J.; Cui, J.; Chen, Y.; Zhu, C.; Liu, F.; Zeng, Q.; Zhou, J.; Yu, P.; Wang, X.; He, H.; Tsang, S. H.; Gao, W.; Suenaga, K.; Ma, F.; Yang, C.; Lu, L.; Yu, T.; Teo, E. H. T.; Liu, G.; Liu, Z. High-Quality Monolayer Superconductor $NbSe_2$ Grown by Chemical Vapour Deposition. *Nat. Commun.* **2017**, *8* (1), 394.
(39) Schmidt, M.; Oppermann, H.; Hennig, C.; Henn, R. W.; Gmelin, E.; Söger, N.; Binnewies, M. Untersuchungen zu Bismutseltenerdoxidhalogeniden der Zusammensetzung Bi_2SEO_4X (X = Cl, Br, I). *Zeitschrift für anorganische und allgemeine Chemie* **2000**, *626* (1), 125−135.
(40) Wasim, S. M.; Rincón, C.; Marín, G.; Bocaranda, P.; Hernández, E.; Bonalde, I.; Medina, E. Effect of Structural Disorder on the Urbach Energy in Cu Ternaries. *Phys. Rev. B* **2001**, *64* (19), No. 195101.
(41) John, J.; Sivaraman, S.; Jaylekshmi, S. Urbach Tail Analysis on the Defect States of Polypyrrole Thin Films Prepared by AC Plasma Polymerization Urbach Tail Analysis on the Defect States of Polypyrrole Thin Films Prepared by AC Plasma Polymerization. *e-Polym.* **2010**, *10* (1), 011.
(42) Makuła, P.; Pacia, M.; Macyk, W. How To Correctly Determine the Band Gap Energy of Modified Semiconductor Photocatalysts Based on UV−Vis Spectra. *J. Phys. Chem. Lett.* **2018**, *9* (23), 6814−6817.
(43) Zhao, Y.; Gao, H.; Huang, R.; Huang, Z.; Li, F.; Feng, J.; Sun, Q.; Dingsun, A.; Yang, H. Precise Determination of Surface Band Bending in Ga-Polar n-GaN Films by Angular Dependent X-Ray Photoemission Spectroscopy. *Sci. Rep* **2019**, *9* (1), 16969.
(44) Mori-Sánchez, P.; Cohen, A. J.; Yang, W. Localization and Delocalization Errors in Density Functional Theory and Implications for Band-Gap Prediction. *Phys. Rev. Lett.* **2008**, *100* (14), No. 146401.
(45) Tao, X.; Shi, W.; Zeng, B.; Zhao, Y.; Ta, N.; Wang, S.; Adenle, A. A.; Li, R.; Li, C. Photoinduced Surface Activation of Semiconductor Photocatalysts under Reaction Conditions: A Commonly Overlooked Phenomenon in Photocatalysis. *ACS Catal.* **2020**, *10* (10), 5941−5948.
(46) Jing, K.; Ma, W.; Ren, Y.; Xiong, J.; Guo, B.; Song, Y.; Liang, S.; Wu, L. Hierarchical Bi_2MoO_6 Spheres in Situ Assembled by Monolayer Nanosheets toward Photocatalytic Selective Oxidation of Benzyl Alcohol. *Applied Catalysis B: Environmental* **2019**, *243*, 10−18.
(47) Frankcombe, T. J.; Liu, Y. Interpretation of Oxygen 1s X-Ray Photoelectron Spectroscopy of ZnO. *Chem. Mater.* **2023**, *35* (14), 5468−5474.
(48) Li, Y.; Chen, H. Facile Fire Treatment of Nanostructured Hematite with an Enhanced Photoelectrochemical Water Splitting Performance. *J. Mater. Chem. A* **2016**, *4* (39), 14974−14977.
(49) Peláez, D. F.; S, J. L. R.; Poznyak, T.; Gutiérrez, H. M.; Adame, J. A. A.; Rojas, L. L.; Torres, C. J. R. Efficient Catalytic Activity of NiO and CeO_2 Films in Benzoic Acid Removal Using Ozone. *RSC Adv.* **2024**, *14* (6), 3923−3935.
(50) Wang, H.; Zhang, H.; Liu, J.; Xue, D.; Liang, H.; Xia, X. Hydroxyl Group Adsorption on GaN (0001) Surface: First Principles and XPS Studies. *J. Electron. Mater.* **2019**, *48* (4), 2430−2437.
(51) Jiang, S.; Li, Y.; Zhang, X.; Li, Y. Enhancing the Photoelectrochemical Water Splitting Activity of Rutile Nanorods by Removal of Surface Hydroxyl Groups. *Catal. Today* **2016**, *259*, 360−367.
(52) Tang, C.; Sun, B.; Li, M.; Zhang, J.; Fan, X.; Gao, F.; Tong, Y.; Dong, L.; Li, Y. Surface Hydroxylated Hematite Promotes Photoinduced Hole Transfer for Water Oxidation. *J. Mater. Chem. A* **2019**, *7* (14), 8050−8054.
(53) Samizo, A.; Minohara, M.; Kikuchi, N.; Ando, K.; Mazuka, Y.; Nishio, K. Disorders and Oxygen Vacancies in P-Type $Sn_2B_2O_7$ (B = Nb, Ta): Role of the B-Site Element. *J. Am. Ceram. Soc.* **2023**, *106* (2), 1540−1546.
(54) Chatterjee, K.; Magnard, N. P. L.; Mathiesen, J. K.; Jensen, K. M. Ø.; Skrabalak, S. E. Local Structure Analysis and Structure Mining for Design of Photocatalytic Metal oxychloride Intergrowths. *J. Mater. Chem. A* **2022**, *43*, 23212.

https://doi.org/10.1021/acs.inorgchem.4c00306
Inorg. Chem. 2024, 63, 8131−8141

NOTE ADDED AFTER ASAP PUBLICATION

Originally published ASAP April 19, 2024; DFT structure solutions added to Supporting Information April 23, 2024.

https://doi.org/10.1021/acs.inorgchem.4c00306
Inorg. Chem. 2024, 63, 8131−8141